THE JOURNAL OF PHYSICAL CHEMISTRY B

Article

pubs.acs.org/JPCB

Effect of Mutation on an Aggregation-Prone Segment of p53: From Monomer to Dimer to Multimer

Atanu Das[†] and Dmitrii E. Makarov*[,†,‡]

[†]Department of Chemistry, University of Texas at Austin, Austin, Texas 78712, United States

[‡]Institute for Computational Engineering and Sciences, University of Texas at Austin, Austin, Texas 78712, United States

Supporting Information

ABSTRACT: Protein aggregation and amyloid formation are implicated in many diseases as well as in other biological phenomena. Recent studies have suggested that amyloid formation of tumor suppressor p53 can lead to loss of its physiological function, resulting in accelerated cancer progression. Design of cancer therapeutics, therefore, requires understanding of the mechanism of p53 aggregation. Here, we have employed atomistic simulations to characterize the aggregation process of the aggregation-prone (as suggested by experimental studies) p53 fragment (LTIITLE, 252−258) and to assess the efficiency of its I254R mutant as an aggregation suppressor. We show that the wild-type sequence attains stable β-sheet rich structure in the parallely arranged dimeric form, which dissociates in a sequential manner under mechanical force. The wild-type sequence further displays high aggregation propensity self-assembling into structures with parallel peptide arrangement. The I254R mutation destabilizes the dimer, changes the mechanical dissociation of the dimer to cooperative unfolding, reduces the aggregation propensity of the sequence, and alters the relative orientation of the peptides in the aggregate. Addition of the wild-type sequence, however, partially restores the aggregation propensity of the I254R mutant.

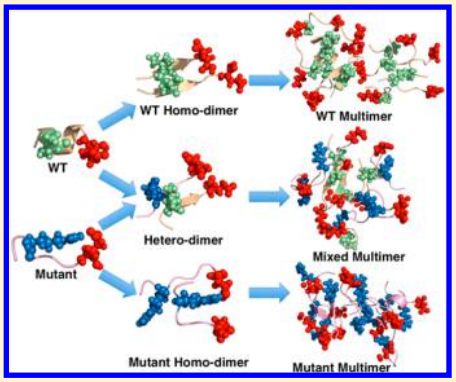

INTRODUCTION

Molecular-level understanding of protein misfolding and aggregation has important biomedical implications. Indeed, these phenomena lead to many life-threating neurodegenerative diseases, including Parkinson's, Alzheimer's, and Huntington's diseases, frontal temporal dementia, amyotrophic lateral sclerosis, and the human prion diseases.[1] More than 24 different proteins and polypeptides have been found to form amyloid deposits *in vivo*, leading to human diseases,[2] but even proteins that are not necessarily implicated in any disease have also been reported to undergo self-assembly leading to amyloid fibrils *in vitro* under certain experimental conditions,[3] suggesting that amyloid fibril formation is a generic property of many proteins and polypeptides.[4] Interestingly, recent reports on the existence of a new class of amyloids that can perform certain biological functions (functional amyloids)[5] have attracted additional attention to the structure and dynamics of amyloids.

The structure of amyloid fibrils is challenging to resolve, as they are insoluble and noncrystalline.[6] Nevertheless, studies that employed X-ray diffraction,[7] solid state NMR,[8] and spectroscopic methods[9] revealed that the arrangement of proteins within fibrils broadly involves cross-β-sheet assemblies, with hydrogen bonds parallel and the β-strands perpendicular to the fibril axis.[6]

The protein p53, also known as TP53 or tumor protein, regulates the cell cycle and functions as a tumor suppressor.[10,11] Amyloid aggregates of both mutant[12] and wild-type[13] p53 are found to be connected with cancers and are believed to be formed following a prion-like mechanism, where specific sequence stretches of p53 initiate the aggregation process and further template the aggregation of the p53, resulting in its loss of function.[14−17] Investigation of the mechanism of aggregation of p53 into amyloid and identification of the fragments of p53 that are involved in amyloid formation is thus key to developing therapeutics against p53's loss of function.

It has been proposed that such aggregation-prone segments in p53 are rich in hydrophobic residues.[14,16,18,19] Specific segments proposed by several groups have similar length and overlap in their sequence location within the complete p53 chain. Specifically, the aggregation propensity of the 250−257 stretch[14] and the 251−257 stretch,[16,19] have been examined theoretically, while a recent experimental study[17] showed the aggregation-prone character of the 252−258 stretch. Interestingly, a single mutation (I254R) of this aggregation-prone sequence can suppress the progression of the fibrillar structure.[17] Motivated by these observations, here we use atomistic simulations to study the aggregation process of 252−258 stretch and of its I254R mutated sequence. Complementary to earlier computational studies of p53 aggregation, which aimed to explain the mechanism of p53 aggregation by characterizing the variety of oligomeric structures encountered

Received: July 25, 2016
Revised: October 12, 2016
Published: October 24, 2016

DOI: 10.1021/acs.jpcb.6b07457
J. Phys. Chem. B 2016, 120, 11665−11673

in the simulations in terms of their secondary structure, interpeptide interactions and free energy landscapes, our work focuses on the stability of the dimer of the aggregation-prone sequence and its mutant; by examining whether the dimer stability is correlated with the aggregation kinetics of multiple segments we then evaluate the proposition that dimer formation can template the aggregation process.

The following specific questions regarding the p53 aggregation pathway are asked here: (1) What is the structure of the monomer and the dimer of the p53 252−258 segment? (2) Which interactions stabilize or destabilize the dimeric form of the wild-type/mutant p53 segment? (3) How does mutation affect the stability of the dimer? (4) Do the monomeric fragments (both wild-type and mutant) aggregate in solution? (5) Does mutation change the structural features of the aggregates?

From the unconstrained simulations of monomers performed here we find that none of the monomeric forms, either wild-type or mutant, shows any β-sheet character. From the analysis of the dimer structures observed in the course of unconstrained dimer simulations we observed the wild-type homodimer to retain a parallel β-sheet structure, in accord with experimental observations,[17] while the mutated homodimer exhibited a deformed conformation with no β-sheet. The heterodimer formed a slightly deformed parallel β-sheet conformation. To further quantify the effect of mutation on dimer stability, we used steered molecular dynamics simulations, which revealed that mutation not only changes the mechanical rupture mechanism from sequential unzipping to simultaneous separation but also significantly lowers the dimer's thermodynamic stability. Starting from random, nonaggregated arrangements of multiple monomers, we have further observed the time evolution of the peptides, allowing us to qualitatively assess how their propensity to aggregate depends on their sequence. Consistent with the lower dimer stability of the mutant, these simulations showed that mutation reduces the aggregation propensity and alters the relative orientation of the peptides in the aggregates.

METHODS

Simulations of the Monomeric Structures. Molecular dynamics simulations were performed using the GROMACS software package, version 4.5.5.[20] Parameters were taken from the CHARMM27 parameter set.[21] Initial structure of the LTIITLE peptide (Pep-I) sequence for the simulation was the experimentally determined amyloid-forming segment LTIITLE from p53 (protein data bank accession code 4RP6).[17] The mutated structure of the 7-residue peptide (LTRITLE, Pep-II) was constructed by mutating the Ile at position 254 to Arg using PyMOL.[22] Peptides were solvated with SPC water molecules in a cubic box so that the minimal distance of the peptide from any edge of the cubic box was at least 1 nm. We note that, although CHARMM is parametrized using TIP3P, the SPC water model was used here for several reasons. First, in addition to reproducing the correct dielectric permittivity, SPC mimics polarizability by changing the dipole moment to adjust to an altered environment (from bulk water to water near polar/hydrophobic parts of proteins). Second, the CHARMM27/TIP3P combination shows larger deviation from the experimental chemical shifts.[23] Third, in comparison to the CHARMM27/SPC combination, CHARMM27/TIP3P displays a stronger bias toward compact, less solvent-exposed, helical conformations.[23]

Electroneutrality of the system was achieved by adding 100 mM NaCl; to achieve this, water molecules were randomly replaced with Na^+ and Cl^- ions at favorable sites (which were identified by computing the electrostatic potential at the site of insertion). There were 3064 water molecules, 7 Na^+ ions, and 6 Cl^- ions in the resulting final composition of Pep-I. For Pep-II, there were 3059 water molecules, 6 Na^+ ions, and 6 Cl^- ions in the resulting final composition. Systems were subjected to steepest descent energy minimization to arrive at conformations with no steric clashes. Each of these minimized conformations was equilibrated in two phases, with position restraints applied to all the heavy atoms throughout. The first phase involved simulating each system for 100 ps under a constant volume (NVT) ensemble at 300 K using the modified Berendsen weak coupling method.[24] The position of the peptide was restrained near the center of the cubic box with a force constant of 1000 kJ mol^{-1} nm^{-2}. Following NVT equilibration, 100 ps of constant pressure (NPT) equilibration was performed, where pressure was maintained isotropically at 1.0 bar using the Parrinello−Rahman barostat;[25] the peptide position was again kept near the center of the cubic box using a harmonic restraint with a force constant of 1000 kJ mol^{-1} nm^{-2}. The two different initial structures were then used to perform 1000.2 ns of NPT constant pressure (1 bar) and constant temperature (300 K) simulation without any constraints. The following parameters were employed in the simulations: the integration time step was 2 fs; snapshots of the trajectories were stored after every 20 ps; the nonbonded interactions list was updated after every 10 steps. The LINCS algorithm[26] was used to constrain all bonds that contained a hydrogen atom to their precise length, with a warning angle of 30°. The peptide, waters, and the two types of ions were coupled to separate temperature baths with a relaxation constant of 0.1 ps. The peptide, waters, and Na^+ and Cl^- ions were coupled separately to constant pressure barostats using Parrinello−Rahman scaling with a relaxation constant of 1.0 ps and 4.5×10^{-5} bar^{-1} isothermal compressibility. All simulations were performed in a cubic cell employing periodic boundary conditions with the standard minimum image convention in all three directions. Long-range electrostatics was treated with the particle mesh Ewald method.[27] The cutoff used for Lennard-Jones interactions was 0.9 nm with 0.12 nm Fourier spacing. The first 0.2 ns of the trajectory was considered as an equilibration period and was omitted from the analysis.

Equilibrium Simulations of the Dimeric Structures. The homodimeric structures of Pep-I and Pep-II in parallel strand arrangements were made from the respective monomeric structures following the crystal structure details given in the article by Soragni et al.[17] In addition, a heterodimer of Pep-I and Pep-II was constructed by mutating one of the Ile254 residues of the homodimeric Pep-I to Arg using PyMOL.[22] The dimer was solvated in a cubic box with SPC water molecules such that the minimum distance of the peptide from any edge of the cubic box was at least 1 nm. There were 3165 water molecules, 8 Na^+ ions, and 6 Cl^- ions in the resulting final composition of homodimeric Pep-I. For the homodimeric Pep-II, there were 3165 water molecules, 6 Na^+ ions, and 6 Cl^- ions in the resulting final composition. For the heterodimer, there were 3166 water molecules, 7 Na^+ ions, and 6 Cl^- ions. Each of the systems was subjected to steepest descent energy minimization to avoid any steric clashes and then to 100 ps NVT simulation at 300 K and to 100 ps NPT simulation at 300 K and at 1 bar. In these simulations, the position of the dimer

DOI: 10.1021/acs.jpcb.6b07457
J. Phys. Chem. B 2016, 120, 11665−11673

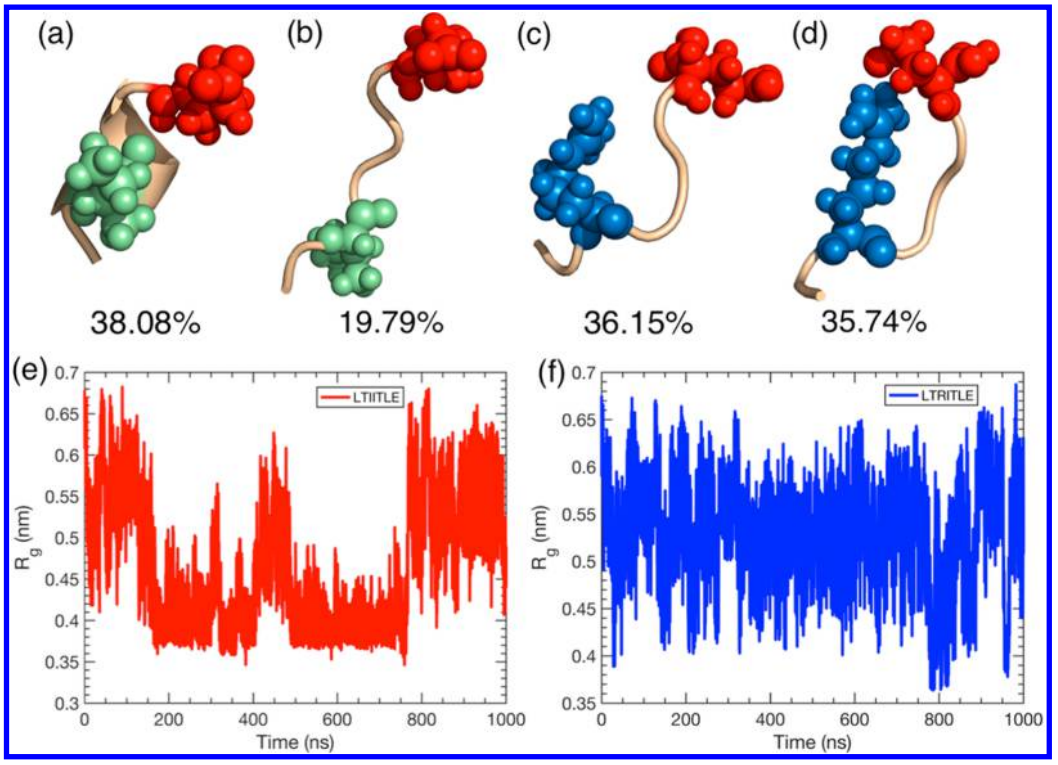

Figure 1. Top panel: clustering analysis of the monomeric forms of Pep-I (a,b) and Pep-II (c,d). The Ile254 (green), Arg254 (blue), and Glu258 (red) residues are shown as spheres, and the rest of the sequence is shown in cartoon representation. Bottom panel: time evolution of the radius of gyration of the two monomeric peptides—(e) Pep-I and (f) Pep-II.

center of mass was restrained near the center of the cubic box using a harmonic restraint with a force constant of 1000 kJ mol^{-1} nm^{-2}. The initial structures obtained this way were used to perform 300.2 ns NPT simulation at P = 1 bar and T = 300 K without any constraints. Other simulation parameters were same as those of the simulations with the monomeric species above. The first 200 ps of each of the trajectories were not included in the analysis, as they were viewed as an equilibration period. Two independent trajectories were simulated for each of the dimeric species. Each trajectory was 300.2 ns in length, with a total simulation time of 600.4 ns for each dimer.

Steered Molecular Dynamics (SMD) Simulations. The equilibrated structures after first 20 ns of the dimer simulations were used for steered molecular dynamics (SMD) simulations. Each of the dimeric structures was solvated in a 2.006 nm × 2.449 nm × 7.035 nm box with SPC water molecules. There were 977 water molecules, 4 Na^+ ions, and 2 Cl^- ions in the resulting final composition of homodimeric Pep-I. For the homodimeric Pep-II, there were 976 water molecules, 2 Na^+ ions, and 2 Cl^- ions in the resulting final composition. For the heterodimer, there were 978 water molecules, 3 Na^+ ions, and 2 Cl^- ions in the resulting final composition. Each of the systems was first subjected to steepest descent energy minimization. An NPT molecular dynamics (100 ps) simulation was performed at 300 K with the Berendsen method for temperature and pressure coupling, and the position of the dimeric construct was maintained near the center of the box by harmonically constraining the system with a force constant of 1000 kJ mol^{-1} nm^{-2}. Throughout the SMD simulations, the position of the center of mass of chain A (COM-A) of the dimer was fixed, and the center of mass of chain B (COM-B) was attached to a harmonic spring with a spring constant of 1000 kJ mol^{-1} nm^{-2} and pulled along the z-axis at a rate of 0.01 nm/ps over a time of 500 ps. The initial and final distances between COM-A and COM-B were 0.48 and 3.48 nm for the homodimeric Pep-I, 0.49 and 3.56 nm for the homodimeric Pep-II, and 0.49 and 3.58 nm for the heterodimer. The peptide, waters, and the two types of ions were separately coupled to a 1 bar Parrinello–Rahman barostat[25] and 300 K Nose-Hoover thermostat.[28,29] The rest of the parameters were the same as those described in the above two cases.

Umbrella Sampling Simulations. Umbrella sampling simulations[30] were used to calculate the free energy profile $G(x)$ as a function of the distance x between the center-of-masses of the two chains within a dimer and to estimate the free energy of binding (ΔG_{bind}) between the chains. Snapshots of the SMD trajectories were used as the initial conditions for the umbrella sampling simulations. In order to achieve better resolution in the regime where the two chains are close to each other, nonuniformly spaced windows were used, with the window spacing Δx being equal to 0.05 nm for x < 2 and 0.1 nm for x > 2 nm. A 100 ns simulation was run for each umbrella window; a harmonic umbrella potential with a spring constant of 1000 kJ mol^{-1} nm^{-2} was used in each window.

Other parameters were the same as those described above. The weighted histogram analysis method (WHAM)[31,32] was used to determine the one-dimensional potential of mean force (PMF) as a function of the dimer separation x. The value of ΔG_{bind} was taken as the difference between the highest and lowest values of the PMF curve. To verify that a 100 ns trajectory was sufficient to obtain equilibrium conformational ensemble within each window, we repeated the analysis using only the first half of each umbrella simulation (50 ns per umbrella window). We find (Figure S1, Table S1) that the resulting values of ΔG_{bind} remain unchanged to within the error bars.

DOI: 10.1021/acs.jpcb.6b07457
J. Phys. Chem. B 2016, 120, 11665–11673

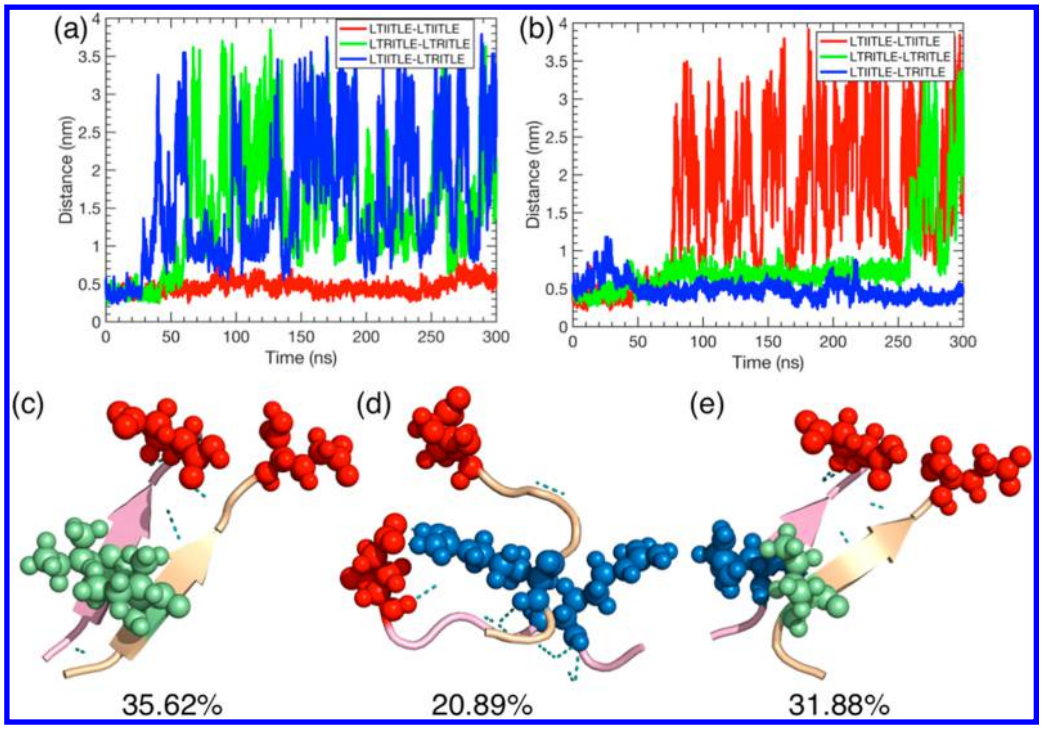

Figure 2. Top panel: time evolution of the distance between the centers of mass of the two strands of the homo- and heterodimers—(a) trajectory set 1 and (b) trajectory set 2. Bottom panel: clustering analysis of (c) Pep-I dimer, (d) Pep-II dimer, and (e) heterodimer. The Ile254 (green), Arg254 (blue), and Glu258 (red) residues are shown as spheres, and the rest of the sequence is shown in cartoon representation. The two monomers of a given dimer are shown is two different colors—chain A in wheat and chain B in pink. The dashed steel-blue lines show the hydrogen bond network present in each configuration.

Simulations of Peptide Aggregation. Twelve copies of the same peptide (for Pep-I and Pep-II) and 6 copies of Pep-I and Pep-II (for the mixed system) were placed separately and randomly in a 7.45 nm × 7.45 nm × 7.45 nm box. The molecules were then solvated with SPC water. The simulation box included 13278 water molecules, 37 Na^+ ions, and 25 Cl^- ions for the Pep-I system; 13269 water molecules, 25 Na^+ ions, and 25 Cl^- ions for the Pep-II system; and 13271 water molecules, 31 Na^+ ions, and 25 Cl^- ions for the mixed system. Steepest descent energy minimization was performed, followed by a 100 ps NVT simulation at 300 K and a 100 ps NPT simulation at 300 K and at 1 bar. In these simulations the center of mass of each individual peptide was harmonically constrained near its initial position using a spring with a force constant of 1000 kJ mol^{-1} nm^{-2}. Finally, a 540.2 ns NPT simulation at T = 300 K and P = 1 bar was performed without any constraints. The rest of the parameters were the same as those of the monomer simulations. The first 0.2 ns of the trajectory were viewed as an equilibration period and were omitted from the analysis.

RESULTS

Most Populated Conformations of the Monomers. Figure 1a–d shows the results of a RMSD-based clustering analysis of the 1 μs trajectories of the monomers of Pep-I and Pep-II, with only the clusters with at least 10% of statistical population shown. The criterion for the clustering analysis was such that if the backbone RMSD between two structures was more than 1 Å after alignment, then they were put in two different clusters. For a given cluster, the representative conformation was generated first by averaging over all the structures present in that cluster, and then performing an energy minimization on that average structure. Dominant structures of Pep-I include a α-helical structure (~38% population, Figure 1a) and an extended conformation (~20% population, Figure 1b), the α-helical conformation being the most populated one. The two dominant clusters of Pep-II show comparable population densities, each with a ~ 36% population, where one cluster exhibits a salt bridge between Arg254 and Glu258 (Figure 1d) and the other does not (Figure 1c).

We further analyzed the dynamics of each monomer by measuring their various structural properties as a function of time. The time evolution of their radii of gyration (R_g) is shown in Figure 1e,f, while similar plots for the backbone root mean square deviation (RMSD) from the initial fully extended β-sheet type conformation, solvent accessible surface area (SASA), and the number of hydrogen bonds are given as Supporting Information (Figure S2a–S2c). Pep-I is observed to reversibly jump between two distinct conformational sub-ensembles, one with an R_g value close 0.38 nm (α-helix, Figure 1a) and the other with an R_g value of 0.55 nm (extended, Figure 1b). Examination of other structural parameters (Figure S2a–S2c) supports the above conclusion. As seen from Figure 1e, the helical conformation of the Pep-I monomer is rather long-lived, with a lifetime of hundreds of nanoseconds, and so a microsecond-long simulated trajectory does not provide a truly equilibrium ensemble; nevertheless it allows us to see reversible transition to and from this helical state. Pep-II exhibits faster structural fluctuations (Figure 1f, Figure S2a–S2c) with multiple instances of the Arg254-Glu258 salt bridge formation and dissociation (Figure S2d). Overall, the MD simulations show that monomeric peptides were flexible in aqueous solution, and a fully extended β-sheet type conformation of

DOI: 10.1021/acs.jpcb.6b07457
J. Phys. Chem. B 2016, 120, 11665–11673

the peptide was not observed for any of the variants. Pep-I, but not Pep-II, showed slight α-helical propensity, within the limits of our simulated time scales.

Unconstrained Simulations of the Dimers. To examine how the conformation of a peptide changes when it comes in contact with another peptide chain in a specific orientation, we have performed unconstrained simulations of peptide dimers. In those simulations the dimers are seen to eventually dissociate, and this dissociation process is irreversible on a time scale of our simulation, and so the thermodynamic stability of each dimer cannot be deduced directly from such simulations. Nevertheless, assuming that local equilibrium is reached during the lifetime of each intact dimer, we can characterize their structure; to further improve sampling we have generated two 300 ns long independent trajectories for each peptide, each starting from an intact dimer structure. For the purpose of displaying the results, these trajectories are organized in 2 sets, each set containing one trajectory per each peptide.

The relative position between the two monomers, as quantified by the distance between their centers of masses, is shown for all six trajectories in Figure 2a,b (see Figures S3−S4 for further structural analysis). In trajectory set 1, Pep-I stayed intact (and the intermonomer distance remained around 0.5 nm) throughout the course of the entire simulation (Figure 2a), but the second trajectory (set 2, Figure 2b) shows dissociation of the same peptide after ∼74 ns. Likewise, the lifetime of the other two dimers varies between two sets of trajectories, with the heterodimer staying intact in the second set. These observations are, of course, not surprising, since the lifetime distribution is expected to be close to exponential. Although a dimer's thermodynamic stability should be correlated with its average lifetime, the combined length of simulated trajectories is insufficient to estimate such lifetimes. At the same time, we can characterize the conformational ensemble of each dimer using the trajectory pieces during which those dimers stayed undissociated. For example, for the Pep-I homodimer such analysis uses the entire trajectory from the first set and the first 74 ns from the second set, etc.

The bottom panel of Figure 2 shows the results of an RMSD-based clustering analysis of the homo- and heterodimers of Pep-I and Pep-II, with only the clusters with at least 10% of statistical population shown. The criterion for the clustering analysis and the method of identification of the representative conformations was the same as for the monomer clustering analysis above. The dominant structure of Pep-I homodimer (∼36%) retains the parallel β-sheet structure (Figure 2c). The representative conformation of the most populated cluster of the heterodimer (∼32%) is similar to that of the Pep-I homodimer, with almost intact parallel β-sheet arrangements (Figure 2e). However, the most dominant cluster of the Pep-II homodimer exhibited a deformed dimer with no β-sheet and with a non-native intermolecular Arg254-Glu258 salt bridge (∼21% population; Figure 2d). The presence of a pair of Arg and a pair of Glu residues in the Pep-II homodimer provided the opportunity to form the observed non-native salt bridge, which disrupted the parallel orientation of the dimer. For the heterodimer, the possibility of forming intra- and/or interpeptide salt bridge(s) was also present, but a salt bridge was not observed in the dominant cluster.

Since the simulation time scales did not allow us to reach equilibrium between the bound and dissociated states of each dimer or to accurately estimate the dimer lifetimes, we resorted to umbrella sampling to estimate the thermodynamic stability of each dimer, as described below.

Mechanical Unfolding of the Dimeric Constructs. Mechanical stability of the dimers provides a measure of the cohesive interactions that keep them together and can both be measured using single-molecule force spectroscopy[33] and estimated through steered molecular dynamics simulations. Thus, motivated, here we report on SMD simulations, where the centers-of-mass of the monomers were pulled apart. The SMD trajectories were further used to generate the initial configurations to be used for the subsequent umbrella sampling calculations.[30]

Figures 3 and 4 show the force profiles and the mechanisms of mechanical unfolding pathways of the dimers, respectively.

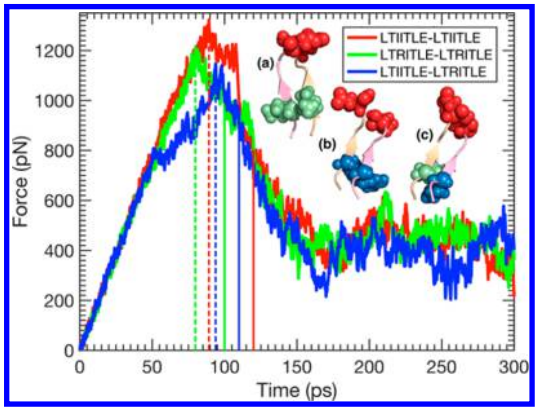

Figure 3. Dissociation force profiles of the dimers. In each case, the dashed vertical line corresponds to the point of maximum force, and the solid vertical line corresponds to the time within which major structural transitions of the dissociation process happened. Equilibrated conformations of the dimers at the beginning of the pulling simulations are shown: (a) Pep-I homodimer, (b) Pep-II homodimer, and (c) heterodimer. The Ile254 (green), Arg254 (blue), and Glu258 (red) residues are shown as spheres and the rest of the sequence is shown in cartoon representation. The two monomers of a given dimer are shown is two different colors—chain A in wheat and chain B in pink.

The first part of the force curves before the rupture event (Figure 3, dashed lines) corresponds to the change in orientation of the dimer, the loss of a few interpeptide hydrogen bonds, and the loss of hydrophobic interactions between the adjacent Leu257 residues of the two monomers (conformations a,b for the Pep-I homodimer, f,g for the Pep-II homodimer, and j,k for the heterodimer in Figure 4). The major peaks of the force curves in Figure 3 correspond to the cooperative rupture of hydrogen bonds and the loss of hydrophobic interactions between a pair of Ile255 (conformations c,d for the Pep-I homodimer, h for the Pep-II homodimer, and l,m for the heterodimer in Figure 4). The last conformation in each row corresponds to the rupture of the rest of the hydrophobic interactions between neighboring Leu252 and/or Ile254 residues of the two monomers (conformations e for the Pep-I homodimer, i for the Pep-II homodimer, and n for the heterodimer in Figure 4). After that, the monomers glide past each other in the direction of the applied force.

Thermodynamic Stability of the Dimeric Structures. The force-time curves obtained via SMD simulations describe mechanical stability of the dimers at a certain pulling rate, but not their thermodynamic stability. To further assess the

DOI: 10.1021/acs.jpcb.6b07457
J. Phys. Chem. B 2016, 120, 11665−11673

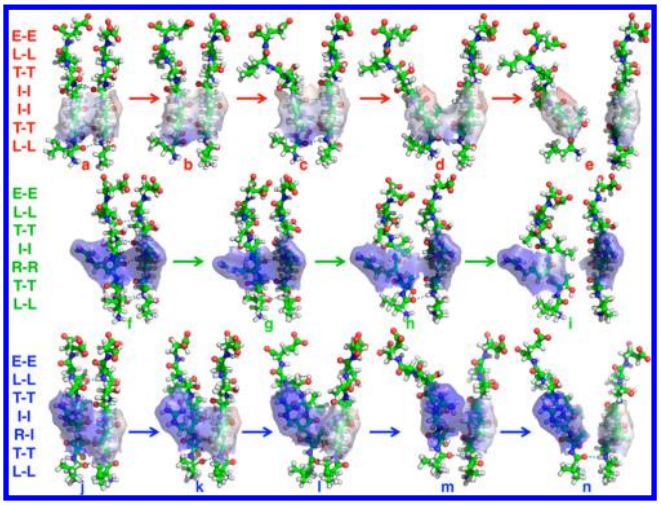

Figure 4. Mechanical unfolding mechanism of the dimeric species. Top: Pep-I homodimer. Middle: Pep-II homodimer. Bottom: heterodimer. The residues are shown in ball-and-stick representation with the electrostatic mapping of residue 254 in each case. The dashed blue lines show the interstrand hydrogen bonds present in each configuration.

cohesive interactions within dimers, we have computed the equilibrium free energies $G(x)$ (also referred to as potentials of mean force or PMF) of the dimers as a function of the intermonomer separation x using umbrella sampling[30] (Figure 5). The free energy ΔG_{bind} of binding was then estimated as the

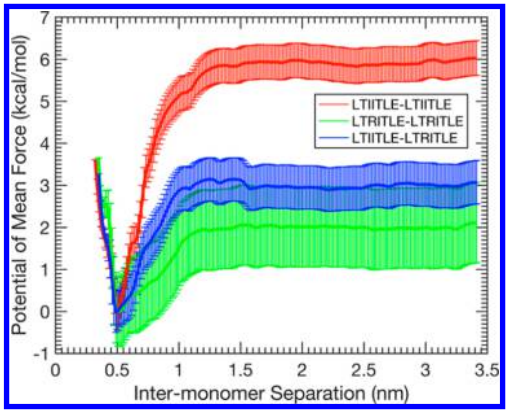

Figure 5. Potentials of mean force for all the three dimers considered in this study. The stability of the Pep-I homodimer is much higher than the other two dimers, the latter having comparable stabilities.

free energy cost to separate the monomers. Error analysis was conducted using a bootstrap method described previously.[34] Of the three dimers, the Pep-I homodimer has the highest thermodynamic stability, with ΔG^{I}_{bind} = 6.03 ± 0.40 kcal/mol. Mutating Ile254 to Arg substantially destabilizes both the Pep-II homodimer (ΔG^{II}_{bind}= 2.11 ± 0.92 kcal/mol) and the heterodimer (ΔG^{H}_{bind} = 3.07 ± 0.50 kcal/mol), with the I254R double mutation (Pep-II homodimer) having a slightly stronger effect than a single mutation (heterodimer). These findings are consistent with the experimental observation that the I254R mutant peptides do not form fibrils.[17]

Spontaneous Aggregation of the Peptides. To probe the aggregation propensity of the wild-type p53 (252−258) (LTIITLE) and its I254R mutant (LTRITLE), we performed all-atom simulations of three systems—one with 12 monomers of the wild-type peptide (Pep-I), one with 12 monomers of the mutated construct (Pep-II), and one with a mixture of 6 Pep-I monomers and 6 Pep-II monomers (mixed)—placed within an explicit solvent box (see Methods Section). As the simulation progressed, peptide clusters formed. To quantify this clustering process, we calculated the number of clusters as a function of simulation time in each case (Figure 6a). A pair of peptides was considered to be in the same cluster if the distance between their centers of masses was less than 1 nm. For the Pep-I and for the mixed systems, the number of distinct clusters decreased nearly monotonically, showing gradual aggregation process (we note that the initial number of clusters is 12, with each peptide being its own "cluster"). In contrast, the number of clusters in the Pep-II showed nonmonotonic behavior, with clusters forming and dissociating (Figure 6a). This observation is consistent with the results from our studies of dimers, which showed that the Pep-II homodimer has the lowest thermodynamic stability.

Interestingly, despite the relatively short time scale of the simulation, all the three systems showed the propensity to form secondary structure, resulting in β-sheet rich aggregates. A more careful analysis of the resulting structures, however, shows qualitative differences between the three cases. Specifically, we measured the relative alignment within pairs of interacting peptides by calculating the angles between their end-to-end vectors. Only those peptides were considered for this analysis whose centers of masses were separated by a distance of no more than 0.5 nm (which roughly corresponds to a typical interpeptide separation within an undissociated dimer—see Figure 2a,b). A negative (positive) value of the cosine of the interpeptide angle then reflects a tendency for antiparallel (parallel) alignment (Figure 6b). The histograms of the cosines of the interpeptide angles shown in Figure 6b suggest that, while the Pep-I aggregates were preferentially oriented in a parallel fashion (similar to the experimentally observed p53 aggregates),[17] both the Pep-II self-assembled clusters and the mixed Pep-I/Pep-II clusters had predominantly antiparallel strand arrangement. Again, this finding is consistent with our analysis of thermodynamic stability of parallel β-sheet dimers, which is much higher for the Pep-I dimer. We further counted the number of conformations encountered in the course of each simulation that had at least two peptides within a distance of 0.5 nm (i.e., the conformations we used in the calculation of distribution of cosine of angles). The fraction of such conformations (measured relative to the total number of conformations encountered in the course of a simulated trajectory) is shown in Figure 6b. This quantity provides another measure of the aggregation propensity, with the wild-type sequence having a much higher value (81%) than the mutated sequence (22%). Interestingly, addition of the wild-type sequence increased the aggregation propensity of the mutated sequence from 22% to 42% without changing the relative orientations of the peptides from antiparallel to parallel. The fact that the mutation reduces the aggregation propensity of the peptide and that the addition of the wild-type sequence partially restores the aggregation propensity of the mutated sequence is further validated by the analysis of the time evolution of the secondary structural features (Figure S5). Of the three systems, the wild-type sequence showed the highest β-sheet content, and there was a rapid decrease in the β-sheet content of the aggregated peptides for the mutated sequence. For the mixed system, however, the β-sheet content was higher

DOI: 10.1021/acs.jpcb.6b07457
J. Phys. Chem. B 2016, 120, 11665−11673

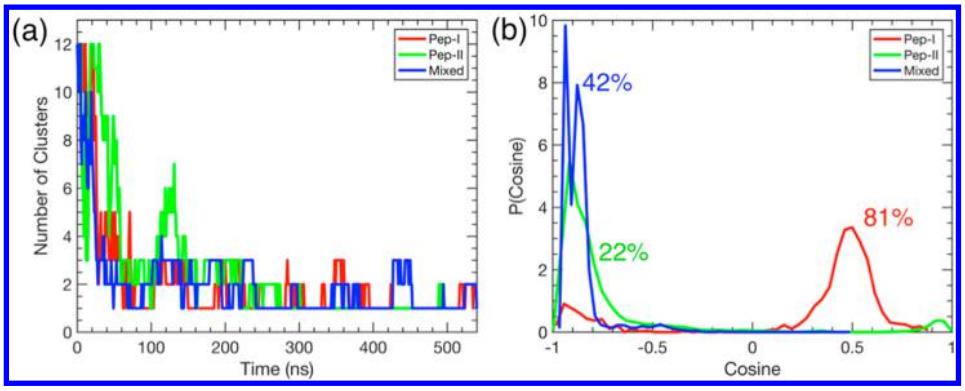

Figure 6. Peptide aggregation. (a) The number of peptide clusters as a function of time. The initial number of clusters is 12, with each peptide being a separate "cluster". (b) Normalized distribution of the cosine of the angle between the end-to-end vectors of all the interacting peptide chains.

than for the mutated sequence, but lower than for the wild-type sequence.

DISCUSSION AND CONCLUSIONS

Formation of amyloid can be viewed as a nucleation and growth process occurring via polymerization,[35,36] which alters soluble native proteins into fibrillar aggregates. Recent experimental studies indicate that, similar to the fibrillar aggregates associated with Alzheimer's and Parkinson's diseases,[37] p53 aggregates may template the aggregation of functional p53 via a prion-like mechanism.[12] Therefore, understanding how p53 aggregates may not only help develop anticancer therapies but also lead to better understanding of the mechanism of protein misfolding and aggregation in general. Recent studies suggested that the aggregation-prone segment of p53 consisting of residues 252−258 initiates the p53 aggregation process[15,17] and that a single mutation of the peptide segment can reduce its aggregation propensity.[17] Yet molecular details of this process remained unknown. In this study, we have elucidated the mechanism of aggregation of the p53 252−258 stretch through molecular dynamics simulations, a theoretical approach that has previously been employed in studies of the molecular basis of peptide and protein aggregation.[38−40] Specifically, we have characterized the structure of the species that can arise in the course of aggregation (monomer, dimer, multimer) and estimated the effect of mutation on aggregation.[16,17] We note that a similar approach of characterizing possible multimeric species occurring in the course of peptide aggregation has been previously employed to characterize monomeric, dimeric, and protofibrillar structures resulting from the aggregation of a tetrapeptide.[41]

We found that the structure of the isolated monomers (Figure 1)[42] undergoes substantial changes when they interact to form a stable β-sheet rich dimer (Figure 2); this is consistent with the observations of the β-sheet structure of the p53 amyloids.[14,16,17] The stabilization of the β-sheet rich conformation of the peptide by dimerization further agrees with the model suggested for amyloid proteins,[43] where misfolded Aβ peptides are stabilized through dimer formation.

We further found that the mutation of Ile by Arg at position 254 significantly alters intermonomer interactions within the dimer, which is evidenced by a change in the mechanical unfolding mechanism (from sequential unzipping to simultaneous unfolding, Figure 4) and in the reduced thermodynamic stability of the dimers (Figure 5). Similar mutation-caused change in the dissociation mechanism of two parallel β-sheets (from sequential to cooperative), as well a reduction in their thermodynamic stability, has been observed for Alzheimer's amyloid protofibrils.[44]

Lower dimer stability caused by mutation implies a decreased tendency to self-associate through the formation of parallel β-sheet structure, in accord with the experimental finding that I254R mutation reduces p53 aggregation.[17] This conclusion is further supported by our simulations of peptide aggregation: While the wild-type peptides were found to predominantly form parallel β-sheet structures (Figure 6b), mutated peptides showed lack of such structure. Similar effect of a single amino acid substitution on the aggregation propensity has also been observed for an amyloid β-protein.[45]

Yet, at least in our simulations, mutation (I254R) did not completely eliminate the aggregation process but showed reduced aggregation propensity with an altered arrangement of the peptides in the aggregated assemblies (parallel to antiparallel) (Figure 6b), presumably via salt bridge formation (Figure 2d). Such stabilization of fibrillar structure by intermolecular salt bridges has previously been observed for Alzheimer's amyloid-β(1−42) fibrils.[46] Moreover, the change in the relative orientation of the β-strands from parallel to antiparallel as a result of a change in hydrophobicity and polarity of the residues in a sequence has also been reported earlier for Aβ peptides.[47] Interestingly, the addition of the wild-type sequence to the mutated system increased the aggregation propensity of the mutated sequence. The observations that mutation (I254R) does not completely eliminate the amyloid prone nature of the sequence and that the wild-type sequence can increase the aggregation propensity of the mutated sequence agree with the results of the recent computational study of the 251−257 fragment of the same protein (ILTIITL) and its mutated sequence.[16] In that study, however, the peptide chains in all three systems—wild-type, mutated, and mixed—showed a preference toward antiparallel orientation for the 251−257 fragment, a behavior somewhat different from what we observed for the 252−258 fragment (parallel orientation for the wild-type system and antiparallel orientation for the mutated and the mixed systems).

ASSOCIATED CONTENT

Supporting Information

The Supporting Information is available free of charge on the ACS Publications website at DOI: 10.1021/acs.jpcb.6b07457.

DOI: 10.1021/acs.jpcb.6b07457
J. Phys. Chem. B 2016, 120, 11665−11673

Convergence test of the estimated binding free energies; structural characterization of the monomeric peptides from unconstrained simulations using backbone RMSD, SASA, and hydrogen bonds; salt bridge formation in the mutated monomeric peptide; structural characterization of the dimeric peptides from unconstrained simulations using backbone RMSD, R_g, and SASA; evolution of secondary structure in peptide aggregation simulations (PDF)

AUTHOR INFORMATION

Corresponding Author

* E-mail: makarov@cm.utexas.edu; Telephone: (512) 471-4575.

Notes

The authors declare no competing financial interest.

ACKNOWLEDGMENTS

Financial support from the Robert A. Welch Foundation (Grant No. F-1514 to DEM) and the National Science Foundation (Grant No. CHE 1266380 to DEM) is gratefully acknowledged. Computational resources were provided by the Texas Advanced Computing Center.

REFERENCES

(1) Dobson, C. M. Principles of Protein Folding, Misfolding and Aggregation. *Semin. Cell Dev. Biol.* **2004**, *15*, 3−16.

(2) Chiti, F.; Dobson, C. M. Protein Misfolding, Functional Amyloid, and Human Disease. *Annu. Rev. Biochem.* **2006**, *75*, 333−366.

(3) Chiti, F.; Webster, P.; Taddei, N.; Clark, A.; Stefani, M.; Ramponi, G.; Dobson, C. M. Designing Conditions for in Vitro Formation of Amyloid Protofilaments and Fibrils. *Proc. Natl. Acad. Sci. U. S. A.* **1999**, *96*, 3590−3594.

(4) Dobson, C. M. The Structural Basis of Protein Folding and Its Links with Human Disease. *Philos. Trans. R. Soc., B* **2001**, *356*, 133−145.

(5) Fowler, D. M.; Koulov, A. V.; Balch, W. E.; Kelly, J. W. Functional Amyloid−from Bacteria to Humans. *Trends Biochem. Sci.* **2007**, *32*, 217−224.

(6) Maji, S. K.; Wang, L.; Greenwald, J.; Riek, R. Structure-Activity Relationship of Amyloid Fibrils. *FEBS Lett.* **2009**, *583*, 2610−2617.

(7) Madine, J.; Jack, E.; Stockley, P. G.; Radford, S. E.; Serpell, L. C.; Middleton, D. A. Structural Insights into the Polymorphism of Amyloid-Like Fibrils Formed by Region 20−29 of Amylin Revealed by Solid-State Nmr and X-Ray Fiber Diffraction. *J. Am. Chem. Soc.* **2008**, *130*, 14990−15001.

(8) Lynn, D. G.; Meredith, S. C. Review: Model Peptides and the Physicochemical Approach to β-Amyloids. *J. Struct. Biol.* **2000**, *130*, 153−173.

(9) Munishkina, L. A.; Fink, A. L. Fluorescence as a Method to Reveal Structures and Membrane-Interactions of Amyloidogenic Proteins. *Biochim. Biophys. Acta, Biomembr.* **2007**, *1768*, 1862−1885.

(10) Harris, S. L.; Levine, A. J. The P53 Pathway: Positive and Negative Feedback Loops. *Oncogene* **2005**, *24*, 2899−2908.

(11) Levine, A. J. P53, the Cellular Gatekeeper for Growth and Division. *Cell* **1997**, *88*, 323−331.

(12) Ano Bom, A. P. D.; Rangel, L. P.; Costa, D. C.; de Oliveira, G. A.; Sanches, D.; Braga, C. A.; Gava, L. M.; Ramos, C. H.; Cepeda, A. O.; Stumbo, A. C.; De Moura Gallo, C. V.; Cordeiro, Y.; Silva, J. L.; et al. Mutant P53 Aggregates into Prion-Like Amyloid Oligomers and Fibrils Implications for Cancer. *J. Biol. Chem.* **2012**, *287*, 28152−28162.

(13) Moll, U. M.; LaQuaglia, M.; Bénard, J.; Riou, G. Wild-Type P53 Protein Undergoes Cytoplasmic Sequestration in Undifferentiated Neuroblastomas but Not in Differentiated Tumors. *Proc. Natl. Acad. Sci. U. S. A.* **1995**, *92*, 4407−4411.

(14) Ghosh, S.; Ghosh, D.; Ranganathan, S.; Anoop, A.; Jha, N. N.; Padinhateeri, R.; Maji, S. K. Investigating the Intrinsic Aggregation Potential of Evolutionarily Conserved Segments in P53. *Biochemistry* **2014**, *53*, 5995−6010.

(15) Goldschmidt, L.; Teng, P. K.; Riek, R.; Eisenberg, D. Identifying the Amylome, Proteins Capable of Forming Amyloid-Like Fibrils. *Proc. Natl. Acad. Sci. U. S. A.* **2010**, *107*, 3487−3492.

(16) Lei, J.; Qi, R.; Wei, G.; Nussinov, R.; Ma, B. Self-Aggregation and Coaggregation of the P53 Core Fragment with Its Aggregation Gatekeeper Variant. *Phys. Chem. Chem. Phys.* **2016**, *18*, 8098−8107.

(17) Soragni, A.; Janzen, D. M.; Johnson, L. M.; Lindgren, A. G.; Nguyen, A. T.-Q.; Tiourin, E.; Soriaga, A. B.; Lu, J.; Jiang, L.; Faull, K. F.; et al. A Designed Inhibitor of P53 Aggregation Rescues P53 Tumor Suppression in Ovarian Carcinomas. *Cancer Cell* **2016**, *29*, 90−103.

(18) Bullock, A. N.; Fersht, A. R. Rescuing the Function of Mutant P53. *Nat. Rev. Cancer* **2001**, *1*, 68−76.

(19) Xu, J.; Reumers, J.; Couceiro, J. R.; De Smet, F.; Gallardo, R.; Rudyak, S.; Cornelis, A.; Rozenski, J.; Zwolinska, A.; Marine, J.-C.; et al. Gain of Function of Mutant P53 by Coaggregation with Multiple Tumor Suppressors. *Nat. Chem. Biol.* **2011**, *7*, 285−295.

(20) Pronk, S.; Páll, S.; Schulz, R.; Larsson, P.; Bjelkmar, P.; Apostolov, R.; Shirts, M. R.; Smith, J. C.; Kasson, P. M.; van der Spoel, D.; et al. Gromacs 4.5: A High-Throughput and Highly Parallel Open Source Molecular Simulation Toolkit. *Bioinformatics* **2013**, *29*, 845−854.

(21) Bjelkmar, P.; Larsson, P.; Cuendet, M. A.; Hess, B.; Lindahl, E. Implementation of the Charmm Force Field in Gromacs: Analysis of Protein Stability Effects from Correction Maps, Virtual Interaction Sites, and Water Models. *J. Chem. Theory Comput.* **2010**, *6*, 459−466.

(22) DeLano, W. L. *The Pymol Molecular Graphics System*; Delano Scientific Llc: Palo Alto, Ca., 2009.

(23) Somavarapu, A. K.; Kepp, K. P. The Dependence of Amyloid-β Dynamics on Protein Force Fields and Water Models. *ChemPhysChem* **2015**, *16*, 3278−3289.

(24) Bussi, G.; Donadio, D.; Parrinello, M. Canonical Sampling through Velocity Rescaling. *J. Chem. Phys.* **2007**, *126*, 014101.

(25) Parrinello, M.; Rahman, A. Polymorphic Transitions in Single Crystals: A New Molecular Dynamics Method. *J. Appl. Phys.* **1981**, *52*, 7182−7190.

(26) Hess, B. P-Lincs: A Parallel Linear Constraint Solver for Molecular Simulation. *J. Chem. Theory Comput.* **2008**, *4*, 116−122.

(27) Darden, T.; York, D.; Pedersen, L. Particle Mesh Ewald: An N·Log (N) Method for Ewald Sums in Large Systems. *J. Chem. Phys.* **1993**, *98*, 10089−10092.

(28) Hoover, W. G. Canonical Dynamics: Equilibrium Phase-Space Distributions. *Phys. Rev. A: At., Mol., Opt. Phys.* **1985**, *31*, 1695.

(29) Nosé, S. A Unified Formulation of the Constant Temperature Molecular Dynamics Methods. *J. Chem. Phys.* **1984**, *81*, 511−519.

(30) Torrie, G. M.; Valleau, J. P. Nonphysical Sampling Distributions in Monte Carlo Free-Energy Estimation: Umbrella Sampling. *J. Comput. Phys.* **1977**, *23*, 187−199.

(31) Hub, J. S.; De Groot, B. L.; Van Der Spoel, D. G_Wham - a Free Weighted Histogram Analysis Implementation Including Robust Error and Autocorrelation Estimates. *J. Chem. Theory Comput.* **2010**, *6*, 3713−3720.

(32) Kumar, S.; Rosenberg, J. M.; Bouzida, D.; Swendsen, R. H.; Kollman, P. A. The Weighted Histogram Analysis Method for Free-Energy Calculations on Biomolecules. I. The Method. *J. Comput. Chem.* **1992**, *13*, 1011−1021.

(33) Lovas, S.; Zhang, Y.; Yu, J.; Lyubchenko, Y. L. Molecular Mechanism of Misfolding and Aggregation of Aβ(13−23). *J. Phys. Chem. B* **2013**, *117*, 6175−6186.

(34) Hub, J. S.; de Groot, B. L. Does CO_2 Permeate through Aquaporin-1? *Biophys. J.* **2006**, *91*, 842−848.

(35) Harper, J. D.; Lansbury, P. T., Jr Models of Amyloid Seeding in Alzheimer's Disease and Scrapie: Mechanistic Truths and Physiological Consequences of the Time-Dependent Solubility of Amyloid Proteins. *Annu. Rev. Biochem.* **1997**, *66*, 385−407.

DOI: 10.1021/acs.jpcb.6b07457
J. Phys. Chem. B 2016, 120, 11665−11673

(36) Jarrett, J. T.; Lansbury, P. T. Seeding "One-Dimensional Crystallization" of Amyloid: A Pathogenic Mechanism in Alzheimer's Disease and Scrapie? *Cell* **1993**, *73*, 1055−1058.
(37) Jucker, M.; Walker, L. C. Self-Propagation of Pathogenic Protein Aggregates in Neurodegenerative Diseases. *Nature* **2013**, *501*, 45−51.
(38) Ma, B.; Nussinov, R. Simulations as Analytical Tools to Understand Protein Aggregation and Predict Amyloid Conformation. *Curr. Opin. Chem. Biol.* **2006**, *10*, 445−452.
(39) Thirumalai, D.; Klimov, D.; Dima, R. Emerging Ideas on the Molecular Basis of Protein and Peptide Aggregation. *Curr. Opin. Struct. Biol.* **2003**, *13*, 146−159.
(40) Wu, C.; Shea, J.-E. Coarse-Grained Models for Protein Aggregation. *Curr. Opin. Struct. Biol.* **2011**, *21*, 209−220.
(41) Bellesia, G.; Shea, J.-E. What Determines the Structure and Stability of Kffe Monomers, Dimers, and Protofibrils? *Biophys. J.* **2009**, *96*, 875−886.
(42) Baumketner, A.; Bernstein, S. L.; Wyttenbach, T.; Bitan, G.; Teplow, D. B.; Bowers, M. T.; Shea, J.-E. Amyloid β-Protein Monomer Structure: A Computational and Experimental Study. *Protein Sci.* **2006**, *15*, 420−428.
(43) Lyubchenko, Y. L.; Kim, B. H.; Krasnoslobodtsev, A. V.; Yu, J. Nanoimaging for Protein Misfolding Diseases. *Wiley Interdiscip. Rev. Nanomed. Nanobiotechnol.* **2010**, *2*, 526−543.
(44) Lemkul, J. A.; Bevan, D. R. Assessing the Stability of Alzheimer's Amyloid Protofibrils Using Molecular Dynamics. *J. Phys. Chem. B* **2010**, *114*, 1652−1660.
(45) Krone, M. G.; Baumketner, A.; Bernstein, S. L.; Wyttenbach, T.; Lazo, N. D.; Teplow, D. B.; Bowers, M. T.; Shea, J.-E. Effects of Familial Alzheimer's Disease Mutations on the Folding Nucleation of the Amyloid β-Protein. *J. Mol. Biol.* **2008**, *381*, 221−228.
(46) Lührs, T.; Ritter, C.; Adrian, M.; Riek-Loher, D.; Bohrmann, B.; Döbeli, H.; Schubert, D.; Riek, R. 3d Structure of Alzheimer's Amyloid-β (1−42) Fibrils. *Proc. Natl. Acad. Sci. U. S. A.* **2005**, *102*, 17342−17347.
(47) Gordon, D. J.; Balbach, J. J.; Tycko, R.; Meredith, S. C. Increasing the Amphiphilicity of an Amyloidogenic Peptide Changes the β-Sheet Structure in the Fibrils from Antiparallel to Parallel. *Biophys. J.* **2004**, *86*, 428−434.

DOI: 10.1021/acs.jpcb.6b07457
J. Phys. Chem. B 2016, 120, 11665−11673